



Published in final edited form as:

Neuron. 2021 May 05; 109(9): 1554–1566.e4. doi:10.1016/j.neuron.2021.03.003.

Single Trial Decoding of Movement Intentions Using Functional Ultrasound Neuroimaging

Sumner L. Norman^{1,*}, David Maresca^{5,*,†}, Vasileios N. Christopoulos^{1,2,*,‡}, Whitney S. Griggs¹, Charlie Demene^{3,4}, Mickael Tanter^{3,4}, Mikhail G. Shapiro^{5,*}, Richard A. Andersen^{1,2,6,*}

¹Biology & Biological Engineering, California Institute of Technology, Pasadena, CA, 91125 USA

²T&C Chen Brain-Machine Interface Center, California Institute of Technology, Pasadena, CA, 91125 USA

³Physics for Medicine Paris, Inserm, CNRS, ESPCI Paris, PSL Research University, 75012 Paris, France

⁴INSERM Technology Research Accelerator in Biomedical Ultrasound, Paris, France

⁵Chemistry & Chemical Engineering, California Institute of Technology, Pasadena, CA, 91125 USA

⁶Lead Contact

Summary

New technologies are key to understanding the dynamic activity of neural circuits and systems in the brain. Here, we show that a minimally invasive approach based on ultrasound can be used to detect the neural correlates of movement planning, including directions and effectors. While non-human primates (NHPs) performed memory-guided movements, we used functional ultrasound (fUS) neuroimaging to record changes in cerebral blood volume with 100 μm resolution. We recorded from outside the dura above the posterior parietal cortex – a brain area important for spatial perception, multisensory integration, and movement planning. We then used fUS signals from the delay period before movement to decode the animals' intended direction and effector. Single trial decoding is a prerequisite to brain-machine interfaces (BMIs) – a key application that

*Correspondence: (mikhail@caltech.edu; richard.andersen@vis.caltech.edu) These authors contributed equally to this work.

†Present affiliation: Imaging Physics, TU Delft, 2628 CJ Delft, The Netherlands

‡Present affiliation: Bioengineering, University of California: Riverside, Riverside, California, USA

*These authors contributed equally to this work

Author Contributions

S.L.N., D.M., V.N.C., M.T., M.G.S. and R.A.A. conceived the study; S.N., D.M., C.D., and M.T. developed the imaging sequences; S.L.N., V.N.C., and W.G. trained the animals. S.L.N., V.N.C., D.M. and W.G. acquired the data; S.L.N., D.M. and V.N.C. performed the data processing; S.L.N., D.M., and V.N.C. drafted the manuscript with substantial contribution from M.G.S. and R.A.A.; all authors edited and approved the final version of the manuscript. M.T., M.G.S. and R.A.A. supervised the research.

Publisher's Disclaimer: This is a PDF file of an unedited manuscript that has been accepted for publication. As a service to our customers we are providing this early version of the manuscript. The manuscript will undergo copyediting, typesetting, and review of the resulting proof before it is published in its final form. Please note that during the production process errors may be discovered which could affect the content, and all legal disclaimers that apply to the journal pertain.

Declaration of Interests

M.T. is a co-founder and shareholder of Iconeus Company which commercializes ultrasonic neuroimaging scanners. D.M. is now affiliated with T.U. Delft, Netherlands. V.C. is now affiliated with University of California, Riverside, USA.

could benefit from this technology. These results are a critical step in the development of neuro-recording and brain interface tools that are less-invasive, high-resolution, and scalable.

eTOC Blurp

Norman et al. uses functional ultrasound (fUS) neuroimaging to record brain activity while animals performed motor tasks. They use fUS signals to predict movement timing, direction, and effector (hand or eye). This is a critical step toward brain recording and interface tools that are less invasive, high-resolution, and scalable.

Introduction

Novel technologies for interfacing with the brain are key to understanding the dynamic activity of neural circuits and systems and diagnosing and treating neurological diseases. Many neural interfaces are based on intracortical electrophysiology, which provides direct access to the electrical signals of neurons with excellent temporal resolution. However, the electrodes must be implanted via significant-risk open-brain surgery. This process causes acute and chronic local tissue damage (Polikov et al., 2005) and implants suffer material degradation over time (Barrese et al., 2013; Kellis et al., 2019). Invasive electrodes are also difficult to scale and limited in sampling density and brain coverage. These factors limit longevity and performance (Kellis et al., 2019; Welle et al., 2020; Woolley et al., 2013). Non-invasive techniques, such as electroencephalography (EEG) and functional magnetic resonance imaging (fMRI), have achieved considerable success in the research setting. Even-so, they are limited by low spatial resolution, summing activity of large brain volumes, and the dispersion of signal through various tissues and bone. Minimally invasive techniques such as epidural electrocorticography (ECoG) span a middle-ground, maintaining relatively high performance without damaging healthy brain tissue (Benabid et al., 2019; Shimoda et al., 2012). However, it is difficult to resolve signals from deep cortical or subcortical structures with spatial specificity. In addition, subdural ECoG remains invasive in requiring penetration of the dura and exposure of underlying brain tissue.

Here, we evaluate the potential of functional ultrasound (fUS) imaging – a recently developed, minimally invasive neuroimaging technique – to provide single-trial decoding of movement intentions, a neural signaling process of fundamental importance and applicability in brain-machine interfaces (BMI). fUS imaging is a hemodynamic technique that visualizes regional changes in blood volume using ultrafast Doppler angiography (Bercoff et al., 2011; Mace et al., 2013; Macé et al., 2011). It provides excellent spatiotemporal resolution compared to existing functional neuroimaging techniques (< 100 μm and 100 ms) and high sensitivity ($\sim 1\text{mm/s}$ velocity (Boido et al., 2019)) across a large field of view (several cm). Since its introduction in 2011 (Macé et al., 2011), fUS has been used to image neural activity during epileptic seizures (Macé et al., 2011), olfactory stimuli (Osmanski et al., 2014), and behavioral tasks in freely moving rodents (Sieu et al., 2015; Urban et al., 2015). It has also been applied to non-rodent species including ferrets (Bimbard et al., 2018), pigeons (Rau et al., 2018), non-human primates (NHPs) (Blaize et al., 2020; Dizeux et al., 2019), and humans (Demene et al., 2017; Imbault et al., 2017; Soloukey et al., 2020). Unlike fMRI, fUS can be applied in freely moving subjects using miniature, head-

mountable transducers (Sieu et al., 2015). In addition, the hemodynamic imaging performance of fUS is approximately 5 to 10-fold better in terms of spatiotemporal resolution and sensitivity compared to fMRI (Deffieux et al., 2018; Macé et al., 2011; Rabut et al., 2020).

In this study, we leveraged the high sensitivity of fUS imaging to detect movement intentions in NHPs. We trained two animals to perform memory-delayed instructed eye movements (saccades) and hand movements (reaches) to peripheral targets. Meanwhile, we recorded hemodynamic activity over the posterior parietal cortex (PPC) through a cranial window throughout the task. PPC is an association cortical region situated between visual and motor cortical areas and is involved in high-level cognitive functions including spatial attention (Colby and Goldberg, 1999), multisensory integration (Andersen and Buneo, 2002), and sensorimotor transformations for movement planning (Andersen and Cui, 2009). The functional characteristics of PPC have been thoroughly studied using electrophysiological (Andersen et al., 1987; Andersen and Buneo, 2002; Colby and Goldberg, 1999; Gnadt and Andersen, 1988; Snyder et al., 1997) and functional magnetic resonance techniques (Kagan et al., 2010; Wilke et al., 2012), providing ample evidence for comparison to the fUS data. PPC contains several sub-regions with anatomical specialization, including the lateral intraparietal area (LIP) involved in planning saccade movements (Andersen et al., 1987; Andersen and Buneo, 2002; Gnadt and Andersen, 1988; Snyder et al., 1997) and the parietal reach region (PRR) involved in planning reach movements (Andersen and Buneo, 2002; Calton et al., 2002; Snyder et al., 2000, 1997). Importantly, their activity can be simultaneously recorded within a single fUS imaging frame (approximate slice volume of 12.8 x 13 x 0.4 mm).

By recording brain activity while animals perform movement tasks, we provide evidence that fUS can detect motor planning activity that precedes movement in NHPs. We extend these results to decode several dimensions of behavior at a single trial level. These include (1) when the monkey entered the task phase, (2) which effector they intended to use (eye or hand), and (3) which direction they intended to move (left or right). These results show for the first time that fUS is capable of imaging hemodynamics in large animals with enough sensitivity to decode the timing and goals of an intended movement. These findings also represent a critical step toward the use of fUS for BMIs. Such interfaces provide a direct causal link between brain and machine by interpreting neural activity related to user intention. They are excellent tools for neuroscientific investigation (Sakellaridi et al., 2019) and as a neuroprosthetic to enable people with paralysis to control assistive devices, including computer cursors and prosthetic limbs (Aflalo et al., 2015; Collinger et al., 2013; Hochberg et al., 2012, 2006). As fUS hardware and software developments enable real-time imaging and processing, fUS may prove a valuable tool for future BMIs.

Results

To look for goal-related hemodynamic signals in the PPC, we acquired fUS images from NHPs using a miniaturized 15 MHz, linear array transducer placed on the dura via a cranial window. The transducer provided a spatial resolution of 100 μm x 100 μm in-plane, slice thicknesses of ~400 μm , covering a plane with a width of 12.8 mm and penetration depth of

16 mm. We positioned the probe surface-normal in a coronal orientation above the PPC (Fig. 1, a–b). We then selected planes of interest for each animal from the volumes available (Fig. 1, c–f). Specifically, we chose planes that captured both the lateral and medial banks of the intraparietal sulcus (*ips*) within a single image and exhibited behaviorally tuned hemodynamic activity. We used a plane-wave imaging sequence at a pulse repetition frequency of 7500 Hz and compounded frames collected from a 500 ms period each second to form power Doppler images with a 1 Hz refresh rate.

Hemodynamic response during memory-guided saccades.

To resolve goal-specific hemodynamic changes within single trials, we trained two NHPs to perform memory-delayed instructed saccades. We used a similar task design to previous experiments investigating the roles of PPC regions using fMRI BOLD (Kagan et al., 2010; Wilke et al., 2012) and reversible pharmacological inactivation (Christopoulos et al., 2015). Specifically, the monkeys were required to memorize the location of a cue presented in either the left or right hemifield and execute the movement once the center fixation cue extinguished (Fig. 2a). The memory phase was chosen to be sufficiently long (from 4.0–5.1 s depending on the animals' training and success rate, mean 4.4 s across sessions) to capture hemodynamic changes. We collected fUS data while each animal (N=2) performed memory-delayed saccades. We collected 2441 trials over 16 days (1209 from Monkey H and 1232 from Monkey L).

We use statistical parametric maps based on the Student's t-test (one-sided with false discovery rate correction) to visualize patterns of lateralized activity in PPC (Fig. 2b, g). We observed event-related average (ERA) changes of CBV throughout the task from localized regions (Fig. 2, c–f, h–i). Spatial response fields of laterally tuned hemodynamic activity appeared on the lateral bank of *ips* (i.e., in LIP). The response fields and ERA waveforms were similar between animals and are consistent with previous electrophysiological (Graf and Andersen, 2014) and fMRI BOLD (Wilke et al., 2012) results. Specifically, ERAs from LIP show higher memory phase responses to contralateral (right) compared to ipsilateral (left) cued trials (one-sided t-test of area under the curve during memory phase, t-test $p < 0.001$).

Monkey H exhibited a similar direction-tuned response in the presumed medial parietal area (MP), a small patch of cortex on the medial wall of the hemisphere (we did not record this area-effect in monkey L because MP was outside the imaging plane). This tuning supports previous evidence of MP's role in directional eye movement observed in a previous study (Thier and Andersen, 1998). In contrast, focal regions of microvasculature outside area LIP also showed strong event-related responses to the task onset but were not tuned to target direction (e.g., Fig. 2e).

Memory delayed reaches.

In a second experiment, we also collected fUS signals while each NHP performed memory reaches. In total, we collected 1480 trials (543 from Monkey H and 937 from Monkey L) over 8 sessions. The task was similar to that of saccades, but the animal's gaze remained fixated throughout the trial, including during the fixation, memory, and reach movement

phases (Fig. 3a). The memory phase ranged from 3.2-5.2 s depending on the animals' training and success rate (mean 4.2 s across sessions). ERAs on the lateral bank of *ips* reveal populations with direction-specific tuning (Fig. 3, c-d, f-g). Area MP, which was responsive to saccade planning for monkey H (Fig. 2i), was not responsive to reach planning. Populations on the medial bank in the putative parietal reach region (PRR) do not exhibit lateralized tuning but do show bilateral tuning to the movement (Fig. 3d, g). These results are consistent with electrophysiological recordings, in which the PRR neurons as a population encode both hemispaces, whereas LIP neurons largely encode the contralateral space (Quiroga et al., 2006).

Single trial decoding.

We predicted the direction of upcoming movements using single trials of fUS data (Fig. 4a). Briefly, we used classwise principal component analysis (CPCA) to reduce data dimensionality. We chose CPCA because it is ideally suited to discrimination problems with high dimension and small sample size (Das and Nenadic, 2009, 2008). We then used ordinary least squares regression (OLSR) to regress the transformed fUS data (from the memory delay period) to the movement direction (i.e., class label). Finally, we used linear discriminant analysis (LDA) to classify the resulting value for each trial as a presumed left or right movement plan. All reported results were generated using a 10-fold cross validation. Saccade direction prediction accuracy within a session (i.e., decoded from the memory delay) ranged from 61.5% (binomial test vs. chance level, $p=0.012$) to 100% ($p<0.001$) on a given 30-minute run. The mean accuracy across all sessions and runs was 78.6% ($p<0.001$). Reach direction prediction accuracy ranged from 73.0% (binomial test vs. chance level, $p<0.001$) to 100% ($p<0.001$). The mean accuracy across all sessions and runs was 88.5% ($p<0.001$).

To analyze the temporal evolution of direction-specific information in PPC, we attempted to decode the movement direction across time through the trial phases: fixation, memory, and movement. For each time point, we accumulated the preceding data. For example, at $t = 2$ s, we included imaging data from $t = 0-2$ s (where $t=0$ s corresponds to the beginning of fixation). The resulting cross-validated accuracy curves (Fig. 4b) show accuracy at chance level during the fixation phase, increasing discriminability during the memory phase, and sustained decode accuracy during the movement phase. During the memory phase, decoder accuracy improved, surpassing significance 2.08 s \pm 0.82 s after the monkey received the target cue for saccades (2.32 s \pm 0.82 s before moving, binomial test vs. chance level, $p<0.05$, Bonferroni corrected for 18 comparisons across time) and 1.92 s \pm 1.4 s for reaches (2.28 s \pm 1.4 s before moving). Decoding accuracy between saccades and reaches was not significantly different.

To determine the amount of data required to achieve maximum decode accuracy, we systematically removed trials from the training set (Fig. 4c). Using just 27 trials, decoder accuracy reached significance for all datasets (binomial test, $p<0.05$) and continued to increase. Decoder accuracy reached a maximum when given 75 trials of training data, on average.

Were we decoding the neural correlates of positions, trajectories, or goals? To answer this question, we used a cross-temporal decoding technique. We used a 1 s sliding window of data to train the decoder and then attempted to decode the intended direction from another 1 s sliding window. We repeated this process for all time points through the trial duration, resulting in an $n \times n$ array of accuracies where n is the number of time windows tested. Cross-validated accuracy was significantly above chance level throughout the memory and movement phases (Fig. 4d, purple line, binomial test vs. chance level, $p < 0.05$, Bonferroni corrected for 18 time points). In other words, the information we're decoding from this brain region was highly similar during movement preparation and execution. This result suggests that this area is encoding movement plans (Snyder et al., 1997), visuo-spatial attention (Colby and Goldberg, 1999), or both. Although intention and attention are overlapping abstract concepts that cannot be separated by this experimental design, dissociating their contribution would not fundamentally change our interpretation. Distinct spatial locations within PPC encoded this information, a fact reflected in the variable weighting assigned to each voxel in our decoding algorithm. The decoder placed the highest weightings in area LIP (Fig. 4e). This also agrees with the canonical function of this region (Andersen and Buneo, 2002; Gnadt and Andersen, 1988).

Decoding memory period, effector, and direction.

To demonstrate the ability of fUS to decode multiple dimensions of behavior from a single trial of data, we trained the same two animals to perform a memory delayed, intermingled effectors task. This task was similar to the saccade and reach tasks in its temporal structure. However, in addition to the animals fixating their gaze during the fixation period, they also moved a joystick to a central cue with their right hand. This cue's color indicated which effector they should move when the go cue arrived: blue for saccades and red for reaches. If the monkey moved the correct effector (eye/hand) to the correct direction (left/right), they received a liquid reward (Fig. 5a). In total, we collected 1576 trials (831 from Monkey H and 745 from Monkey L) over four sessions (two from each animal) while they performed this task.

We decoded the temporal course of (a) the task structure, (b) the effector, and (c) the target direction of the animal using a decision tree decoder. First, we predicted the task memory periods vs. non-memory periods (including movement, ITI, fixation, etc.). We refer to this distinction as task/no-task (Fig. 5c, task/no-task). To predict when the monkey entered the memory period, the decoder used continuous data where each power Doppler image was labeled as task or no-task. After predicting the animal entered the task phase, the second layer of the decision tree used data from the predicted task phase period to classify effector and direction (Fig. 5c, reach/saccade, left/right). Each of these decodes used the same strategy as before: cross-validated CPCA. Fig. 5b depicts the confusion matrix of decoding accuracy for each class for monkeys H and L. The classifier correctly predicted no-task periods 85.9% and 88.8% of the time for Monkeys H and L, respectively, left vs. right on 72.8% and 81.5% of trials for Monkeys H and L, and eye vs. hand on 65.3% and 62.1% of trials for Monkeys H and L. All three decodes were significantly above chance level ($p < 0.05$, binomial test vs. chance, Bonferroni corrected for three comparisons).

Vascular signal and information content.

Purported benefits of fUS compared to established neuroimaging techniques are increased resolution and sensitivity. To test the benefit of increased resolution, we classified movement goals while systematically decreasing the resolution of the image. We resized the images using a low-pass filter in each of the dimensions of the imaging plane: x – across the probe surface and z – with image depth. We then used the entire image – where the downsized images contained fewer pixels – to decode movement direction. Accuracy continuously decreased as voxel sizes increased (Fig. 6a). This effect was isotropic, i.e., similar for both x and z directions.

We hypothesized that functional information useful for decoding would primarily be located in sub-resolution (<100 μm) vessels within the imaging plane. This hypothesis was based on the function of hyperemia, which starts in parenchymal arterioles and first order capillaries; i.e., vessels of diameter < 50 μm (Rungta et al., 2018). To test this hypothesis, we rank ordered voxels by their mean power Doppler intensity and segmented them by deciles, resulting in a spatial map of ranked deciles (Fig. 6c). Deciles 1-2 mostly captured sub-cortical areas. Deciles 3-8 mostly captured cortical layers. Deciles 9 and 10 were largely restricted to large arteries, commonly on the cortical surface and in the sulci. We then classified movement goals using data from each decile. We normalized accuracy for each session where 0 represents chance level (50%) and 1 represents the maximum accuracy reached across deciles. Accuracy peaked when the regions of the image within the 3rd decile of mean Doppler power were used to decode movement direction. This decile was mostly represented by cortex vasculature, much of which is at or below the limits of fUS resolution. This result is consistent with our hypothesis that functional hyperemia arises from sub-resolution vessels (Boido et al., 2019; Maresca et al., 2020) and agrees with previous studies in rodents (Demené et al., 2016) and ferrets (Bimbard et al., 2018).

Discussion

Contributions compared to previous work.

This work presents a high-water mark for ultrasound neuroimaging sensitivity that builds on the two previous studies of fUS in non-human primates. Significant advances include (1) classification of behavior using fUS data from a single trial, (2) detection of the neural correlates of behavior before its onset, (3) the first investigation of motor planning using fUS, and (4) significant advances in ultrafast ultrasound imaging for single trial and real-time imaging as a precursor to BMI. Dizeux et al. 2019 were the first to use fUS in NHPs, finding changes in CBV in the supplementary eye field (SEF) during an eye movement task and mapping directional functional connectivity within cortical layers (Dizeux et al., 2019). Blaize et al., 2020 recorded fUS images from the visual cortex (V1, V2, V3) of NHPs to reconstruct retinotopic maps (Blaize et al., 2020). Both studies explored the boundaries of fUS sensitivity. Dizeux et al. showed that the correlation of fUS signal from SEF and the behavior signal was statistically predictive of the success rate of the animal. However, this prediction required 40 s of data. Blaize et al. used a binary classification (50% chance level) technique to determine the number of trials necessary to construct retinotopic maps. They reached 89% accuracy after 10 averaged trials for one monkey and 91.8% for the second

monkey. This study is the first to successfully classify fUS activity with just a single trial of data. Furthermore, we predicted the differences between multiple task variables (e.g., effector, direction) in addition to detecting the task itself. We also decoded the behavior of the animal *before* it was executed. Compared to previous multi-trial detection of a stimulus or task, detecting cognitive state variables from single trials represents a new high bar for fUS neuroimaging. This study represents the first investigation of motor planning and execution using fUS. It thus represents the first example in a future body of work using fUS to study the neural correlates of motor learning and motor control in large animals. Finally, the methods developed here are technological achievements by introducing minimal latency (Supplementary video 1, Fig. S1) and being robust across animals and task paradigms (Figs. 2–5). Thus, they can be applied in a range of tasks and applications that require real-time signal detection.

Simultaneous effector and direction decoding.

PPC's location within the dorsal stream suggests that while visuospatial variables are well represented, other movement variables such as effector may be more difficult to detect. Indeed, decoding accuracy was higher for direction, i.e., left vs. right, than for effector, i.e., hand vs. eye (Fig. 5b). The observed difference in performance is likely due to PPCs bias toward the contralateral side and partially intermixed populations for effectors in some regions. In addition to direction and effector, we decoded the task vs. no-task phases. This is a critical step toward closed-loop feedback environments such as BMI where the user gates their own movement or the decoder is otherwise not privy to movement or task timing information. Furthermore, simultaneous decoding of task state, direction, and effector are a promising step forward for the use of fUS in both complex behaviors and BMIs.

Comparison of fUS to electrophysiology.

There are several clear advantages of fUS monitoring. fUS can reliably record from large portions of the brain simultaneously (e.g., cortical areas LIP and PRR) with a single probe. fUS is also much less invasive than intracortical electrodes; it does not require penetration of the dura mater. This is a significant attribute because it greatly reduces the risk level of the technique. Furthermore, while tissue reactions degrade the performance of chronic electrodes over time (Woolley et al., 2013), fUS operates epidurally, precluding these reactions. In addition, our approach is highly adaptive thanks to the reconfigurable electronic focusing of the ultrasound beam and its wide field of view. This makes it much easier to target regions of interest. fUS also provides access to cortical areas deep within sulci and subcortical brain structures that are exceedingly difficult to target with electrophysiology. Finally, the mesoscopic view of neural populations made available by fUS may be favorable for decoder generalization. Thus, training and using decoders across days and/or subjects will be an exciting and important direction of future research.

Other techniques, such as non-invasive scalp EEG, have been used to decode single trials and as a neural basis for control of BMI systems (Norman et al., 2018; Wolpaw et al., 1991; Wolpaw and McFarland, 2004). The earliest proof-of-concept EEG-based BMI achieved a one-bit decode (Nowlis and Kamiya, 1970). Performance of modern EEG BMIs varies greatly across users (Ahn and Jun, 2015), but can yield two degrees of freedom with 70-90%

accuracy (Huang et al., 2009). This performance is comparable to that described here using fUS. However, fUS performance is rapidly increasing as an evolving neuroimaging technique, including recent breakthroughs in 3D fUS neuroimaging (Rabut et al., 2019; Sauvage et al., 2018). These technological advances are likely to herald improvements in fUS single-trial decoding and future BMIs.

Epidural ECoG is a minimally invasive technique used for neuroscientific investigation, clinical diagnostics, and as a recording method for BMIs. Building on the success of more-invasive subdural ECoG, early epidural ECoG in monkeys enabled decoding of continuous 3D hand trajectories with slightly worse accuracy than subdural ECoG (Shimoda et al., 2012). More recently, bilateral epidural ECoG over human somatosensory cortex facilitated decoding of 8 degrees of freedom (4 degrees of freedom per arm including 3D translation of a robotic arm and wrist flexion) with ~70% accuracy (Benabid et al., 2019). In this study, we demonstrated that unilateral fUS imaging of PPC enabled 3 degrees of freedom with similar accuracy. This is fewer degrees than attainable using modern bilateral ECoG grids. However, it demonstrates that, as a young technique, fUS holds excellent potential. Future work can, for example, extend these findings to similarly record bilateral cortical and subcortical structures, such as M1, PPC, and basal ganglia. As fUS recording technology rapidly advances toward high speed, wide coverage, 3D scanning, these types of recordings will become commonplace.

Advances in fUS technology.

Improvements in fUS imaging and computation power continue to accelerate functional frame rates and sensitivity. New scanner prototypes promise faster refresh rates, already reaching 6 Hz (Brunner et al., 2020). Although high temporal resolutions will oversample the hemodynamic response, they enable detection of new feature types; for example, directional mapping of functional connectivity between brain regions (Dizeux et al., 2019). The user could also preferentially sacrifice frame rate to compound more frames into functional images, improving image sensitivity. Thus, we anticipate that – although these results are a critical step in decoding brain states from a single trial – they are only the first in many forthcoming improvements.

Goal decoding for BMI.

The results presented here suggest that fUS has potential as a recording technique for BMI. A potential limitation is the temporal latency of the hemodynamic response to neural activity. Electrophysiology-based BMIs that decode velocity of intended limb movements require as little latency as possible. However, in many cases, goal decoding circumvents the need for instantaneous updates. For example, if a BMI decodes the visuospatial location of a goal (as we do here), the external effector, e.g., a robotic arm, can complete the movement without low level, short-latency information, e.g., joint angles. Furthermore, goal information as found in PPC can represent sequences of consecutive movements (Baldauf et al., 2008) and multiple effectors simultaneously (Chang and Snyder, 2012). Finally, future goal decoders could potentially leverage information from regions in the ventral stream to decode object semantics directly (Bao et al., 2020). These unique advantages of goal decoding could thus improve BMI efficacy without requiring short-latency signals.

fUS BMI in its form in the current study could also enable BMIs outside the motor system. Optimal applications might require access to deep brain structures or large fields of view on time scales compatible with hemodynamics. For example, cognitive BMIs such as state decoding of mood and other psychiatric states (Shanechi, 2019) are of great interest due to the astounding prevalence of psychiatric disorders. Like fUS, cognitive BMI is a small but rapidly advancing area of research (Andersen et al., 2019; Musallam et al., 2004). It is our mission that these areas of research mature together as they are well matched in time scale and spatial coverage.

One concern about goal decoding is that an error and subsequent change in motor plan happens on short timescales. These sudden changes are difficult to decode regardless of recording methodology, only recently appearing as a potential feature in chronically-implanted electrophysiology-based BMIs (Even-Chen et al., 2017). Action inhibition is often attributed to subcortical nuclei, e.g. the basal ganglia (Jin and Costa, 2010) and the subthalamic nucleus (Aron et al., 2016), rather than the cortical areas most often used for BMI. fUS may be able to simultaneously image cortex and these subcortical nuclei but would still be subject to hemodynamic delays. Decreasing system latencies and detecting error signals with complementary methods will be an important topic for future research.

Activity in posterior parietal cortex during saccade planning.

Activation maps revealed regions (~100 μ m to ~1 cm) within PPC during saccade planning that were more responsive to contralateral targets than ipsilateral targets. Contralateral tuning of these regions during memory-delay is consistent with the findings from previous fMRI studies (Kagan et al., 2010; Wilke et al., 2012). Our results are also consistent with the extensive evidence from electrophysiological recordings in NHPs that show LIP is involved in planning and executing saccadic movements (Quiroga et al., 2006; Snyder et al., 1997). Notably, the ERA waveforms display significantly larger target-specific differences compared to fMRI signals in a memory-delayed saccade task, i.e., 2-5% vs 0.1-0.5% (Kagan et al., 2010; Wilke et al., 2012), and have much finer spatial resolution. This sensitivity was possible despite the deepest sub-regions of interest extending 16 mm below the probe surface. At this depth, signal attenuation is approximately -7.2 dB (assuming uniform tissue using a 15 MHz probe). Using a probe with a lower center frequency would allow for increasing depths at the cost of spatiotemporal resolution. Use of microbubbles (Errico et al., 2016) or biomolecular contrast agents (Maresca et al., 2020) may enhance hemodynamic contrast allowing for deeper imaging without sacrificing resolution.

In addition to well-studied PPC subregions, we also identified patches of activity in the medial parietal area (MP) located within medial parietal area PG (PGm) (Pandya and Seltzer, 1982). These functional areas were much smaller in size and magnitude than those nearer to the *ips*. This may be one potential reason why MP activity was not reported in previous fMRI studies. However, electrophysiological studies have showed that stimulation of this area can elicit goal-directed saccades, indicating its role for eye movements (Thier and Andersen, 1998). The addition of the hemodynamic results presented here are the first hemodynamic evidence of MP function. A limitation of this finding is that we did not observe such activity in the second animal, likely because MP was not in the imaging plane.

Current efforts to develop 3D fUS imaging (Rabut et al., 2019) will eliminate this limitation, allowing us to identify new areas based on response properties.

Activity in posterior parietal cortex during reach planning.

We also collected data during a memory-delayed reaching task. ERA waveforms identified increases in CBV during the memory phase for regions on the medial aspect of the *ips*. The parietal reach region (PRR) is located on the medial bank of the *ips* and is characterized by functional selectivity to effector; i.e., the arm (Christopoulos et al., 2015). The responses we observed in this area were effector specific; they did not appear in the saccadic data. However, they were not direction specific; increases in CBV activity were present for left-cued *and* right-cued trials. This bilateral reach response can be explained by the spatial scale of the recording method. Whereas single unit electrophysiology in PRR reveals single neurons that are tuned to contralateral hand movement planning, a significant portion of PRR neurons are also tuned to ipsilateral movement planning (Quiroga et al., 2006). Within the limits of fUS resolution (~100 μm), each voxel records the hemodynamic response to the summed activity of neurons within the voxel (~100 μm x 100 μm x 400 μm) Therefore, our results, in the context of previous literature, provide evidence that 1) populations of ipsilaterally- and contralaterally-tuned neurons were roughly equivalent, and 2) these populations are mixed at sub-resolution scales (100 μm). We also found activity on the lateral bank of *ips* that encoded target direction for an upcoming reach. That is, responses were more robust to contralateral targets. Although this area is predominantly involved in saccade movements, neurophysiological studies have also reported neurons within the LIP area that encode reaches to peripheral targets (Colby and Duhamel, 1996; Snyder et al., 1997). This area was located more ventral to saccade related areas in the lateral bank of *ips* and may be within the ventral intraparietal area (VIP). VIP is a bimodal visual and tactile area (Duhamel et al., 1998) that produces movements of the body when electrically stimulated (Cooke et al., 2003; Thier and Andersen, 1996), consistent with a possible role in reaching movements.

Instructed vs. free movement.

We decoded activity as the monkeys performed instructed movements rather than internally driven ('free') movements. A previous study using fMRI showed that free-choice movements produced similar activation patterns in LIP; however, the difference in signal between left/right targets was smaller than that for instructed movements (Wilke et al., 2012). Given the improvement in signal made possible with fUS, it may be possible to decode movement direction from single trials of free-choice movements, although accuracy may be impacted. As free-choice movements are more conducive to BMI use, this is an important direction for future research.

Conclusions

The contributions presented here required significant advancements in large-scale recording of hemodynamic activity with single-trial sensitivity. Decoding capabilities are competitive with existing and mature techniques, establishing fUS as a technique for neuroscientific investigation in task paradigms that require single-trial analysis, real time neurofeedback, or

BMI. Although the neurophysiology presented here is in NHPs, we expect that the methods described will transfer well to human neuroimaging, single-trial decoding, and eventually, BMI. We first described the visuomotor planning function of PPC using electrophysiology in NHPs (Gnadt and Andersen, 1988; Snyder et al., 1997) and later PPC electrophysiology-based BMI control (Aflalo et al., 2015; Sakellaridi et al., 2019). Translation of these findings into human neuroimaging and BMI is an important direction of future study. In addition to its utility for neuroscientific investigation, brain-machine interfacing (BMI) is a promising technique to restore movement to people living with neurological injury and disease. The advancements presented here are a critical first step in ushering in a new era of BMIs that are less-invasive, high-resolution, and scalable. These tools will empower researchers to make unique insights into the function and malfunction of brain circuits, including neurological injury and disease. Furthermore, future work advancing these findings could make a large impact in neuroprosthetics by developing and disseminating high-performance, minimally invasive BMIs.

STAR Methods

Resource Availability

Lead Contact—Further information and requests for resources should be directed to and will be fulfilled by the Lead Contact, Richard A. Andersen (richard.andersen@vis.caltech.edu).

Materials Availability—This study did not generate new unique materials.

Data and Code Availability—Data and analysis software to replicate the primary results will be shared upon request from Sumner Norman (sumnern@caltech.edu).

Experimental model and subject details

We implanted two healthy adult male rhesus macaques (*Macaca mulatta*) weighing 10–13 kg. All surgical and animal care procedures were done in accordance with the National Institutes of Health Guide for the Care and Use of Laboratory Animals and were approved by the California Institute of Technology Institutional Animal Care and Use Committee.

Method details

Animal preparation and implant—We implanted two animals with polyether ether ketone head caps anchored to the skull with titanium screws. We then placed a custom polyether ketone (Monkey H) or stainless-steel (Monkey L) head holder on the midline anterior aspect of the cap. Finally, we placed a unilateral square chamber of 2.4 cm inner diameter, made of polyetherimide (Monkey H) or nylon (Monkey L) over a craniotomy above the left intraparietal sulcus. The dura underneath the craniotomy was left intact. To guide the placement of the chamber, we acquired high-resolution (700 μm) anatomical MRI images before the surgery using a Siemens 3T MR scanner, with fiducial markers to register the animals' brains to stereotaxic coordinates.

Behavioral setup—During each recording session, the monkeys were placed in a dark anechoic room. They sat in a custom designed primate chair, head fixed, facing an LCD monitor ~30 cm away. Visual stimuli were presented using custom Python software based on PsychoPy (Peirce, 2009). Eye position was monitored at 60 Hz using a miniature infrared camera (Resonance Technology, Northridge, CA, USA) and ViewPoint pupil-tracking software (Arrington Research, Scottsdale, AZ, USA). Reaches were performed using a 2-dimensional joystick (Measurement Systems). Both eye and cursor positions were recorded simultaneously with the stimulus and timing information and stored for offline access. Data analysis was performed in Matlab 2020a (MathWorks, Natick, MA, USA) using standard desktop computers.

Behavioral tasks—The animals performed memory-guided eye movements to peripheral targets (Fig. 2a). Each trial started with a fixation cue (red diamond; 1.5 cm side length) presented in the center of screen (fixation period). The animal fixated for 5.35-6.33 s depending on training (mean 5.74 s across sessions). Then, a single cue (red diamond; 1.5 cm side length) appeared either on the left or the right hemifield for 200 ms, indicating the location of the target. Both targets were located equidistantly from the central fixation cue (23° eccentricity). After the cue offset, the animals were required to remember the location of the targets while maintaining eye fixation (memory period). This period was chosen to be sufficiently long to capture hemodynamic transients. The memory period was consistent within each session but varied across sessions from 4.02-5.08 s (mean 4.43 s across session) depending on the animal's level of training. Once the central fixation cue disappeared (i.e., go signal) the animals performed a direct eye movement (saccade) within 500 ms to the remembered location of the target. If the eye position arrived within a radius of 5° of the targets, it was re-illuminated and stayed on for the duration of the hold period (1 s). If the animal broke eye fixation before the go signal (i.e., shifted their gaze outside of a window of 7.5 cm, corresponding to 14° of visual angle) the trial was aborted. Successful trials were followed by a liquid reward. The fixation and memory periods were subject to 400 ms of jitter sampled from a uniform distribution to preclude the animal from anticipating the change(s) of the trial phase.

Both animals also performed memory-guided reach movements to peripheral targets using a 2-dimensional joystick positioned in front of the chair with the handle at knee level. Each trial started with two fixation cues presented at the center of the screen. The animal fixated his eyes on the red diamond cue (1.5 cm side length) and acquired the green cue by moving a square cursor (0.3 cm side length) controlled by his right hand on the joystick (fixation period). The animal fixated for 2.53-5.85 s depending on training (mean 3.94 s across sessions). Then, a single green target (1.5 cm side length) was presented either on the left or the right visual field for a short period of time (300 ms). After the cue offset, the animal was required to remember the location of the targets for a memory period while maintaining eye and hand fixation. The memory period was consistent within each session but varied across sessions from 3.23-5.20 (mean 4.25 s across session). Once the central green cue disappeared, the animal performed a direct reach to the remembered target location within 500 ms, without breaking eye fixation. If they moved the cursor to the correct goal location, the target was re-illuminated and stayed on for duration of the hold period (1 s). Targets

were placed at the same locations as in saccade trials. If the cursor moved out of the target location, the target was extinguished, and the trial was aborted. Any trial in which the animal broke eye fixation or initiated a reaching movement before the go signal or failed to arrive at the target location was aborted. Successful trials were followed with the same liquid reward as in saccade trials. The fixation and memory periods were subject to 400 ms of jitter sampled from a uniform distribution to preclude the animal from anticipating the change(s) of the trial phase.

We also trained both animals on a task that intermingled memory delayed saccades and reaches (Fig. 5a). Similar to the reach task, each trial started with two fixation cues presented at the center of the screen: one for his eyes and one for his right hand. The target sizes were maintained from the reach task. The key difference was that the color of the gaze fixation diamond was randomized as blue or red: blue to cue saccades and red to cue reaches. After a 4.3 s memory period, a single white target (1.5 cm side length) was presented either on the left or right visual field for a short period of time (300 ms). After the cue offset, the animal was required to remember the location of the targets for the duration of the memory period. The memory period across all sessions for both monkeys was 4.0 s. Once the central green cue disappeared, the animal performed a saccade or reach via joystick to the remembered target location within 500 ms, without breaking fixation of the non-cued effector. If they moved the cursor to the correct goal location, the target was re-illuminated and stayed on for the duration of the hold period (1 s). If the cued effector moved out of the target location, the target was extinguished, and the trial was aborted. Any trial in which the animal broke fixation of the non-cued effector or initiated a movement of the cued effector before the go signal or failed to arrive at the target location was aborted. Successful trials were followed with the same liquid reward as in saccade and reach trials. The fixation and memory periods were subject to 400 ms of jitter sampled from a uniform distribution to preclude the animal from anticipating the change(s) of the trial phase.

Functional Ultrasound sequence and recording—During each recording session, we placed the ultrasound probe (128 elements linear array probe, 15.6 MHz center frequency, 0.1 mm pitch, Vermon, France) in the chamber with acoustic coupling gel. This enabled us to acquire images from the posterior parietal cortex (PPC) with an aperture of 12.8 mm and depths up to 23 mm (results presented here show up to 16 mm depth). This large field of view allowed us to image several PPC regions simultaneously. These superficial and deep cortical regions included, but were not limited to, area 5d, lateral intraparietal (LIP) area, medial intraparietal (MIP) area, medial parietal area (MP), and ventral intraparietal (VIP) area.

We used a programmable high-framerate ultrasound scanner (Vantage 128 by Verasonics, Kirkland, WA) to drive a 128-element 15 MHz probe and collect the pulse echo radiofrequency data. We used a plane-wave imaging sequence at a pulse repetition frequency of 7500 Hz. We transmitted plane waves at tilted angles of -6 to 6° in 3° increments. We then compounded data originating from each angle to obtain one high-contrast B-mode ultrasound image (Mace et al., 2013). Each high-contrast B-mode image was formed in 2 ms, i.e., at a 500 Hz framerate.

Regional changes in cerebral blood volume induced by neurovascular coupling can be captured by ultrafast power Doppler ultrasound imaging (Macé et al., 2011). We implemented an ultrafast power Doppler sequence using a spatiotemporal clutter-filter to separate blood echoes from tissue backscattering. We formed Power Doppler images of the NHP brain using 250 compounded B-mode images collected over 0.5 s. Image formation and data storage were performed after the pulse sequence and took ~0.5 s. Thus, the pulse sequence and image formation/save resulted in power Doppler functional mapping of the NHP brain at a 1 Hz refresh rate.

Anatomical PPC regions were spatially located by their stereotaxic positions from the pre-surgical MRI. Response of these functional areas was confirmed by mapping activated voxels obtained during the experimental phase of this work. If necessary, the imaging plane was adjusted to record the most responsive area. Each acquisition consisted of 900-3600 blocks of 250 frames where each block represented 1 second of data (equivalent to 15-60 minutes runtime). Finally, we stored the in-phase and quadrature sampled data to high-speed solid-state drive memory for offline processing.

Power Doppler image processing—We used singular value decomposition to discriminate red blood cell motion from tissue motion and extracted the Doppler signal in each ensemble of 250 coherently compounded frames (Demené et al., 2015; Montaldo et al., 2009). The resulting images were then stored in a 3D array of 2D images in time series. In some experiments, we observed motion of the entire imaging frame. These shifts were indicative of a change in the position of the probe/tissue interface due to uncommonly forceful movements of the animal. We corrected for these events using rigid-body image registration based on the open source NoRMCorre package (Pneumatikakis and Giovannucci, 2017), using an empirical template created from the first 20 frames from the same session. We also tested nonrigid image registration but found little improvement, confirming that motion observed was due to small movements between the probe/dura interface rather than changes in temperature or brain morphology.

Quantification and statistical analysis

All analyses were performed using MATLAB 2020a.

ERA waveforms and statistical parametric maps—We display event-related average (ERA) waveforms (Fig. 2, c–f, h–i; Fig. 3, c–d, f–g) of power Doppler change as percentage change from baseline. The baseline consists of the three seconds preceding the first Doppler image obtained after the directional cue was given on any given trial. ERA waveforms are represented as a solid line with surrounding shaded areas representing the mean and standard deviation. We generated activation maps (Fig. 2, b, g; Fig. 3b, e) by performing a one-sided t-test for each voxel individually with false discovery rate (FDR) correction based on the number of voxels tested. In this test, we compared the area under the curve of the change in power Doppler during the memory phase of the event-related response. The movement direction represented the two conditions to be compared, and each trial represented one sample for each condition. We chose a one-sided test because our hypothesis was that contralateral movement planning would elicit *greater* hemodynamic responses in LIP

compared to ipsilateral planning (based on canonical LIP function). This has the added benefit of being easily interpretable: areas of activation represent contralateral tuning. Voxels with values of $p < 0.01$ are displayed as a heat map overlaid on a background vascular map for anatomical reference.

Single trial decoding—Decoding single trial movement intention involved three parts: 1) aligning CBV image time series with behavioral labels, 2) feature selection, dimensionality reduction and class discrimination, and 3) cross validation and performance evaluation (Fig. 4a). First, we divided the imaging dataset into event aligned responses for each trial, i.e., 2D Power Doppler images through time for each trial. We then separated trials into a training set and testing set according to a 10-fold cross validation scheme. The training set was attached to class labels that represented the behavioral variable being decoded. For example, movement direction would be labeled left or right. The test set was stripped of such labels. Features were selected in the training set by ranking each voxel's q-value comparing the memory phase responses to target direction in the training data. Direction-tuned voxels (FDR corrected for number of pixels in image, $q < 0.05$) of up to 10% of the total image were kept as features. We also tested selecting features by drawing regions of interest around relevant anatomical structures e.g., LIP. Although this method can outperform q-maps, it is more laborious and depends on user skill, so we do not present its results here. For the intermingled effector task, we used all features (i.e., the whole image) because it did not require combining multiple t-maps. For dimensionality reduction and class separation, we used classwise principal component analysis (CPCA) and linear discriminant analysis (LDA) (Das and Nenadic, 2009), respectively. This decoding method has been implemented with success in many real-time BMIs (Do et al., 2013, 2011; King et al., 2015; Wang et al., 2019, 2012), and is especially useful in applications with high dimensionality. CPCA computes the principal components (PCs) in a piecewise manner individually for training data of each class. We retained principal components to account for >95% of variance. We improved class separability by running linear discriminant analysis (LDA) on the CPCA-transformed data. Mathematically the transformed feature for each trial can be represented by $f = T_{LDA} \Phi_{CPCA}(d)$, where $d \in \mathbb{R}^1$ are the flattened imaging data for a single trial, Φ_{CPCA} is the piecewise linear CPCA transformation, and T_{LDA} is the LDA transformation. Φ_{CPCA} is physically related to space and time and thus can be viewed within the context of physiological meaning (Fig. 4e). We subsequently used Bayes rule to calculate the posterior probabilities of each class given the observed feature space. Because CPCA is a piecewise function, this is done twice, once for each class, resulting in four posterior likelihoods: $P_L(L|f^*)$, $P_L(R|f^*)$, $P_R(L|f^*)$, $P_R(R|f^*)$, where f^* represents the observation, P_L and P_R represent the posterior probabilities in the CPCA subspaces created with training data from left-directed and right-directed trials, respectively. Finally, we store the optimal PC vectors and corresponding discriminant hyperplane from the subspace with the highest posterior probability. We then used these findings to predict the behavioral variable of interest for each trial in the testing set. That is, we compute f^* from fUS imaging data for each trial in the testing set to predict the upcoming movement direction. Finally, we rotate the training and testing sets according to k-fold validation, storing the BMI performance metrics for each iteration. We report the mean decoding accuracy as a percentage of correctly predicted trials (Fig. 4b). In measures across multiple sessions where an independent variable is being tested

(e.g., number of trials in training set), we use a normalized accuracy that is linearly scaled to [0, 1] where 0 is chance level (50%) and 1 is the maximum accuracy across the set of values used in the independent variable (e.g., Fig. 4c). This was necessary to regularize raw accuracy values across multiple sessions and animals.

Analysis of training set sample size—As BMI models increase in complexity, their need for data also increases. To demonstrate the robustness of our piecewise linear decoding scheme to limited data, we systematically reduced the amount of data used in the training set (Fig. 4c). We used $N-i$ trials in the training set and i trials in the testing set in a cross-validated manner, rotating the training/testing set i times for $i = 1, 2, \dots, N-10$. We stop at $N-10$ because accuracy was diminished to chance level and when less than 10 trials are used in the training set, it becomes increasingly likely that there will be an under- or non-represented class, i.e., few or no trials to one of the movement directions. We report the mean normalized accuracy standard error of the means (SEM) across both animals and all recording sessions as a function of the number of trials in the training set ($N-i$) (Fig. 4c).

Multicoder for intermingled effectors task—For the intermingled effectors task (Fig. 5), we used the same decoding scheme described above to decode effector and direction. However, instead of using data from the period defined by the experiment, we used a decision tree to define the task period. That is, we first predicted the memory period from the non-memory periods (i.e., task epoch vs. no-task epoch). To do this, we labeled each frame of fUS in the training set with a label for task or no-task. We then decoded each frame in the testing set using the same decoding scheme described above. The primary difference of note here is that we used individual frames of data rather than cumulative frames from within a known task period. We then refined these predictions by assuming that any time the classifier predicted the animal had entered a task state, they would be in that task state for three seconds. This allowed us to use three seconds' worth of data to train and decode the effector and direction variables. Note that while the task/no-task classifier makes a prediction every 1 s, the effector and direction make a prediction for each trial defined by the task/no-task classifier.

Cross temporal decoding—We also performed an analysis to determine the nature of hemodynamic encoding in PPC using a cross-temporal decoding technique. In this analysis, we used all temporal combinations of training and testing data, using a one second sliding window. We used 1 s of data from all trials to train the decoder and then attempted to decode from each of the 1 s windows of testing data throughout the trial. We then updated the training window and repeated the process. This analysis results in an $n \times n$ array of accuracy values where n is the number of time windows in the trial. We report the 10-fold cross-validated accuracies as a percentage of correctly predicted trials (Fig. 4d). To assess the statistical significance of these results, we used a Bonferroni corrected binomial test vs. chance level (0.5) where the number of comparisons was n^2 . We overlaid a contour at $p=0.05$ to indicate the temporal boundaries of significant decoding accuracies.

Decoding with reduced spatial resolution—Part of the motivation for using fUS is its spatial resolution. To test the effects of increased resolution, we synthetically reduced the

resolution of the in-plane imaging data using a Gaussian filter. We performed this analysis at all combinations of x and z direction (width and depth, respectively) starting at true resolution (i.e., 100 μm) up to a worst-case of 5 mm resolution. We report the 10-fold cross-validated accuracy values as a function of these decreasing resolutions as a 2D heat map and as 1D curves of mean accuracy in both the x and z directions with shaded areas representing s.e.m. (Fig. 6a). A limitation of this approach is that we cannot downsample the out-of-plane dimension. Thus, the reported accuracy values are likely higher than those attainable by a technique with isotropic voxel size, e.g., fMRI.

Decoding with different time windows—To analyze the effect of cumulative vs. fixed length decoders, we used different sliding windows of data (1 s, 2 s, 3 s) to decode upcoming movement direction (left or right) using data from the memory delay period. We report these results using accuracy as a function of trial time and the maximum accuracy achieved during the memory period for each session (Fig. 6b). Accuracies are represented at each time point through the fixation and memory periods using data aligned to the end of the time bin used for decoding. For example, an accuracy at $t=3$ s for a decoder using 3 s of data represents a result trained on data from $t = 0-3$ s. To assess significance between different conditions, we used a student's two-tailed t-test.

Power Doppler quantiles—We also investigated the source of hemodynamic information content by segmenting the images according to their mean power Doppler signal as a proxy for mean cerebral blood flow within a given area. Specifically, we segmented the image into deciles by mean power Doppler signal within a session, where higher deciles represented higher power and thus higher mean blood flow (Fig. 6c). Deciles were delineated by the number of voxels, i.e., the number of voxels was the same within each segment and did not overlap. Using only the voxels within each decile segment, we computed the mean accuracy for each recording session. We report the mean normalized accuracy across all recording sessions (Fig. 4c) where shaded error bars represent SEM.

Supplementary Material

Refer to Web version on PubMed Central for supplementary material.

Acknowledgements

We thank Kelsie Pejsa for assistance with animal care, surgeries, and training. We thank Thomas Deffieux for his contributions to the ultrasound neuroimaging methods that made this work possible. We thank Igor Kagan for assisting in implantation planning. Finally, we thank Krissta Passanante for her illustrations. SN was supported by a Della Martin Postdoctoral Fellowship. DM was supported by a Human Frontiers Science Program Cross-Disciplinary Postdoctoral Fellowship (Award No. [LT000637/2016](#)). WG was supported by the UCLA-Caltech MSTP (NIGMS T32 GM008042). This research was supported by the National Institute of Health BRAIN Initiative (grant [U01NS099724](#) to MGS), the T&C Chen Brain-machine Interface Center, and the Boswell Foundation (to RAA).

References

- Aflalo T, Kellis S, Klaes C, Lee B, Shi Y, Pejsa K, Shanfield K, Hayes-Jackson S, Aisen M, Heck C, 2015. Decoding motor imagery from the posterior parietal cortex of a tetraplegic human. *Science* 348, 906–910. [PubMed: 25999506]

- Ahn M, Jun SC, 2015. Performance variation in motor imagery brain–computer interface: A brief review. *J. Neurosci. Methods* 243, 103–110. 10.1016/j.jneumeth.2015.01.033 [PubMed: 25668430]
- Andersen R, Essick G, Siegel R, 1987. Neurons of area 7 activated by both visual stimuli and oculomotor behavior. *Exp. Brain Res* 67, 316–322. [PubMed: 3622691]
- Andersen RA, Aflalo T, Kellis S, 2019. From thought to action: The brain–machine interface in posterior parietal cortex. *Proc. Natl. Acad. Sci* 116, 26274–26279. 10.1073/pnas.1902276116
- Andersen RA, Buneo CA, 2002. Intentional maps in posterior parietal cortex. *Annu. Rev. Neurosci* 25, 189–220. [PubMed: 12052908]
- Andersen RA, Cui H, 2009. Intention, action planning, and decision making in parietal-frontal circuits. *Neuron* 63, 568–583. [PubMed: 19755101]
- Aron AR, Herz DM, Brown P, Forstmann BU, Zaghoul K, 2016. Frontosubthalamic circuits for control of action and cognition. *J. Neurosci* 36, 11489–11495. [PubMed: 27911752]
- Baldauf D, Cui H, Andersen RA, 2008. The Posterior Parietal Cortex Encodes in Parallel Both Goals for Double-Reach Sequences. *J. Neurosci* 28, 10081–10089. 10.1523/JNEUROSCI.3423-08.2008 [PubMed: 18829966]
- Bao P, She L, McGill M, Tsao DY, 2020. A map of object space in primate inferotemporal cortex. *Nature* 583, 103–108. 10.1038/s41586-020-2350-5 [PubMed: 32494012]
- Barrese JC, Rao N, Paroo K, Triebwasser C, Vargas-Irwin C, Franquemont L, Donoghue JP, 2013. Failure mode analysis of silicon-based intracortical microelectrode arrays in non-human primates. *J. Neural Eng* 10, 066014. [PubMed: 24216311]
- Benabid AL, Costecalde T, Eliseyev A, Charvet G, Verney A, Karakas S, Foerster M, Lambert A, Morinière B, Abroug N, 2019. An exoskeleton controlled by an epidural wireless brain–machine interface in a tetraplegic patient: a proof-of-concept demonstration. *Lancet Neurol.* 18, 1112–1122. [PubMed: 31587955]
- Bercoff J, Montaldo G, Loupas T, Savery D, Mézière F, Fink M, Tanter M, 2011. Ultrafast compound Doppler imaging: Providing full blood flow characterization. *IEEE Trans. Ultrason. Ferroelectr. Freq. Control* 58, 134–147. [PubMed: 21244981]
- Bimbard C, Demene C, Girard C, Radtke-Schuller S, Shamma S, Tanter M, Boubenec Y, 2018. Multi-scale mapping along the auditory hierarchy using high-resolution functional UltraSound in the awake ferret. *Elife* 7, e35028. [PubMed: 29952750]
- Blaize K, Arcizet F, Gesnik M, Ahnine H, Ferrari U, Deffieux T, Pouget P, Chavane F, Fink M, Sahel J-A, Tanter M, Picaud S, 2020. Functional ultrasound imaging of deep visual cortex in awake nonhuman primates. *Proc. Natl. Acad. Sci* 117, 14453–14463. 10.1073/pnas.1916787117 [PubMed: 32513717]
- Boido D, Rungta RL, Osmanski B-F, Roche M, Tsurugizawa T, Le Bihan D, Ciobanu L, Charpak S, 2019. Mesoscopic and microscopic imaging of sensory responses in the same animal. *Nat. Commun* 10, 1–13. [PubMed: 30602773]
- Brunner C, Grillet M, Sans-Dublanc A, Farrow K, Lambert T, Macé E, Montaldo G, Urban A, A Platform for Brain-wide Volumetric Functional Ultrasound Imaging and Analysis of Circuit Dynamics in Awake Mice. *Neuron* 0. 10.1016/j.neuron.2020.09.020
- Calabrese E, Badea A, Coe CL, Lubach GR, Shi Y, Styner MA, Johnson GA, 2015. A diffusion tensor MRI atlas of the postmortem rhesus macaque brain. *Neuroimage* 117, 408–416. [PubMed: 26037056]
- Calton JL, Dickinson AR, Snyder LH, 2002. Non-spatial, motor-specific activation in posterior parietal cortex. *Nat. Neurosci* 5, 580–588. [PubMed: 12021766]
- Chang SWC, Snyder LH, 2012. The representations of reach endpoints in posterior parietal cortex depend on which hand does the reaching. *J. Neurophysiol* 107, 2352–2365. 10.1152/jn.00852.2011 [PubMed: 22298831]
- Christopoulos VN, Bonaiuto J, Kagan I, Andersen RA, 2015. Inactivation of parietal reach region affects reaching but not saccade choices in internally guided decisions. *J. Neurosci* 35, 11719–11728. [PubMed: 26290248]
- Colby CL, Duhamel J-R, 1996. Spatial representations for action in parietal cortex. *Cogn. Brain Res*
- Colby CL, Goldberg ME, 1999. Space and attention in parietal cortex. *Annu. Rev. Neurosci* 22, 319–349. [PubMed: 10202542]

- Collinger JL, Wodlinger B, Downey JE, Wang W, Tyler-Kabara EC, Weber DJ, McMorland AJ, Velliste M, Boninger ML, Schwartz AB, 2013. High-performance neuroprosthetic control by an individual with tetraplegia. *The Lancet* 381, 557–564.
- Cooke DF, Taylor CS, Moore T, Graziano MS, 2003. Complex movements evoked by microstimulation of the ventral intraparietal area. *Proc. Natl. Acad. Sci* 100, 6163–6168. [PubMed: 12719522]
- Das K, Nenadic Z, 2009. An efficient discriminant-based solution for small sample size problem. *Pattern Recognit.* 42, 857–866.
- Das K, Nenadic Z, 2008. Approximate information discriminant analysis: A computationally simple heteroscedastic feature extraction technique. *Pattern Recognit.* 41, 1548–1557.
- Deffieux T, Demene C, Pernot M, Tanter M, 2018. Functional ultrasound neuroimaging: a review of the preclinical and clinical state of the art. *Curr. Opin. Neurobiol* 50, 128–135. [PubMed: 29477979]
- Demene C, Baranger J, Bernal M, Delanoe C, Auvin S, Biran V, Alison M, Mairesse J, Harribaud E, Pernot M, 2017. Functional ultrasound imaging of brain activity in human newborns. *Sci. Transl. Med* 9, eaah6756. [PubMed: 29021168]
- Demené C, Deffieux T, Pernot M, Osmanski B-F, Biran V, Gennisson J-L, Sieu L-A, Bergel A, Franqui S, Correas J-M, 2015. Spatiotemporal clutter filtering of ultrafast ultrasound data highly increases Doppler and fUltrasound sensitivity. *IEEE Trans. Med. Imaging* 34, 2271–2285. [PubMed: 25955583]
- Demené C, Tiran E, Sieu L-A, Bergel A, Gennisson JL, Pernot M, Deffieux T, Cohen I, Tanter M, 2016. 4D microvascular imaging based on ultrafast Doppler tomography. *NeuroImage* 127, 472–483. 10.1016/j.neuroimage.2015.11.014 [PubMed: 26555279]
- Dizeux A, Gesnik M, Ahnine H, Blaize K, Arcizet F, Picaud S, Sahel J-A, Deffieux T, Pouget P, Tanter M, 2019. Functional ultrasound imaging of the brain reveals propagation of task-related brain activity in behaving primates. *Nat. Commun* 10, 1400. [PubMed: 30923310]
- Do AH, Wang PT, King CE, Abiri A, Nenadic Z, 2011. Brain-computer interface controlled functional electrical stimulation system for ankle movement. *J. Neuroengineering Rehabil* 8, 49.
- Do AH, Wang PT, King CE, Chun SN, Nenadic Z, 2013. Brain-computer interface controlled robotic gait orthosis. *J. Neuroengineering Rehabil* 10, 111.
- Duhamel J-R, Colby CL, Goldberg ME, 1998. Ventral intraparietal area of the macaque: congruent visual and somatic response properties. *J. Neurophysiol* 79, 126–136. [PubMed: 9425183]
- Errico C, Osmanski B-F, Pezet S, Couture O, Lenkei Z, Tanter M, 2016. Transcranial functional ultrasound imaging of the brain using microbubble-enhanced ultrasensitive Doppler. *NeuroImage* 124, 752–761. [PubMed: 26416649]
- Even-Chen N, Stavisky SD, Kao JC, Ryu SI, Shenoy KV, 2017. Augmenting intracortical brain-machine interface with neurally driven error detectors. *J. Neural Eng* 14, 066007. 10.1088/1741-2552/aa8dc1 [PubMed: 29130452]
- Gnadt JW, Andersen RA, 1988. Memory related motor planning activity in posterior parietal cortex of macaque. *Exp. Brain Res* 70, 216–220. [PubMed: 3402565]
- Graf AB, Andersen RA, 2014. Brain-machine interface for eye movements. *Proc. Natl. Acad. Sci* 111, 17630–17635. [PubMed: 25422454]
- Hochberg LR, Bacher D, Jarosiewicz B, Masse NY, Simeral JD, Vogel J, Haddadin S, Liu J, Cash SS, van der Smagt P, 2012. Reach and grasp by people with tetraplegia using a neurally controlled robotic arm. *Nature* 485, 372–375. [PubMed: 22596161]
- Hochberg LR, Serruya MD, Friehs GM, Mukand JA, Saleh M, Caplan AH, Branner A, Chen D, Penn RD, Donoghue JP, 2006. Neuronal ensemble control of prosthetic devices by a human with tetraplegia. *Nature* 442, 164–171. [PubMed: 16838014]
- Huang D, Lin P, Fei D-Y, Chen X, Bai O, 2009. Decoding human motor activity from EEG single trials for a discrete two-dimensional cursor control. *J. Neural Eng* 6, 046005. 10.1088/1741-2560/6/4/046005 [PubMed: 19556679]
- Imbault M, Chauvet D, Gennisson J-L, Capelle L, Tanter M, 2017. Intraoperative functional ultrasound imaging of human brain activity. *Sci. Rep* 7, 7304. [PubMed: 28779069]
- Jin X, Costa RM, 2010. Start/stop signals emerge in nigrostriatal circuits during sequence learning. *Nature* 466, 457–462. [PubMed: 20651684]

- Kagan I, Iyer A, Lindner A, Andersen RA, 2010. Space representation for eye movements is more contralateral in monkeys than in humans. *Proc. Natl. Acad. Sci* 107, 7933–7938. [PubMed: 20385808]
- Kellis S, Rieth L, Baker B, Bashford L, Pejsa KW, Lee B, Liu C, 2019. Quantitative scanning electron microscopy analysis of intracortical microelectrode arrays after five years in human neocortex, in: Society for Neuroscience. Presented at the Neuroscience, Chicago, IL.
- King CE, Wang PT, McCrimmon CM, Chou CC, Do AH, Nenadic Z, 2015. The feasibility of a brain-computer interface functional electrical stimulation system for the restoration of overground walking after paraplegia. *J. Neuroengineering Rehabil* 12, 80.
- Macé E, Montaldo G, Cohen I, Baulac M, Fink M, Tanter M, 2011. Functional ultrasound imaging of the brain. *Nat. Methods* 8, 662–664. [PubMed: 21725300]
- Mace E, Montaldo G, Osmanski B-F, Cohen I, Fink M, Tanter M, 2013. Functional ultrasound imaging of the brain: theory and basic principles. *IEEE Trans. Ultrason. Ferroelectr. Freq. Control* 60, 492–506. [PubMed: 23475916]
- Maresca D, Payen T, Lee-Gosselin A, Ling B, Malounda D, Demené C, Tanter M, Shapiro MG, 2020. Acoustic biomolecules enhance hemodynamic functional ultrasound imaging of neural activity. *NeuroImage* 209, 116467. [PubMed: 31846757]
- Montaldo G, Tanter M, Bercoff J, Benech N, Fink M, 2009. Coherent plane-wave compounding for very high frame rate ultrasonography and transient elastography. *IEEE Trans. Ultrason. Ferroelectr. Freq. Control* 56, 489–506. [PubMed: 19411209]
- Musallam S, Corneil B, Greger B, Scherberger H, Andersen R, 2004. Cognitive control signals for neural prosthetics. *Science* 305, 258–262. [PubMed: 15247483]
- Norman SL, McFarland DJ, Miner A, Cramer SC, Wolbrecht ET, Wolpaw JR, Reinkensmeyer DJ, 2018. Controlling pre-movement sensorimotor rhythm can improve finger extension after stroke. *J. Neural Eng* 15, 056026. [PubMed: 30063219]
- Nowlis DP, Kamiya J, 1970. The Control of Electroencephalographic Alpha Rhythms Through Auditory Feedback and the Associated Mental Activity. *Psychophysiology* 6, 476–484. 10.1111/j.1469-8986.1970.tb01756.x [PubMed: 5418812]
- Osmanski B-F, Martin C, Montaldo G, Lanière P, Pain F, Tanter M, Gurden H, 2014. Functional ultrasound imaging reveals different odor-evoked patterns of vascular activity in the main olfactory bulb and the anterior piriform cortex. *Neuroimage* 95, 176–184. [PubMed: 24675645]
- Pandya DN, Seltzer B, 1982. Intrinsic connections and architectonics of posterior parietal cortex in the rhesus monkey. *J. Comp. Neurol* 204, 196–210. 10.1002/cne.902040208 [PubMed: 6276450]
- Peirce JW, 2009. Generating stimuli for neuroscience using PsychoPy. *Front. Neuroinformatics* 2, 10.
- Pnevmatikakis EA, Giovannucci A, 2017. NoRMCorre: An online algorithm for piecewise rigid motion correction of calcium imaging data. *J. Neurosci. Methods* 291, 83–94. [PubMed: 28782629]
- Polikov VS, Tresco PA, Reichert WM, 2005. Response of brain tissue to chronically implanted neural electrodes. *J. Neurosci. Methods* 148, 1–18. [PubMed: 16198003]
- Quiroga RQ, Snyder LH, Batista AP, Cui H, Andersen RA, 2006. Movement intention is better predicted than attention in the posterior parietal cortex. *J. Neurosci* 26, 3615–3620. [PubMed: 16571770]
- Rabut C, Correia M, Finel V, Pezet S, Pernot M, Deffieux T, Tanter M, 2019. 4D functional ultrasound imaging of whole-brain activity in rodents. *Nat. Methods* 1–4. [PubMed: 30573832]
- Rabut C, Yoo S, Hurt RC, Jin Z, Li H, Guo H, Ling B, Shapiro MG, 2020. Ultrasound Technologies for Imaging and Modulating Neural Activity. *Neuron* 108, 93–110. 10.1016/j.neuron.2020.09.003 [PubMed: 33058769]
- Rau R, Kruizinga P, Mastik F, Belau M, de Jong N, Bosch JG, Scheffer W, Maret G, 2018. 3D functional ultrasound imaging of pigeons. *Neuroimage* 183, 469–477. [PubMed: 30118869]
- Rungta RL, Chaigneau E, Osmanski B-F, Charpak S, 2018. Vascular compartmentalization of functional hyperemia from the synapse to the pia. *Neuron* 99, 362–375. [PubMed: 29937277]
- Sakellaridi S, Christopoulos VN, Aflalo T, Pejsa KW, Rosario ER, Ouellette D, Pouratian N, Andersen RA, 2019. Intrinsic Variable Learning for Brain-Machine Interface Control by Human Anterior

- Intraparietal Cortex. *Neuron* 102, 694–705.e3. 10.1016/j.neuron.2019.02.012 [PubMed: 30853300]
- Sauvage J, Flesch M, Ferin G, Nguyen-Dinh A, Poree J, Tanter M, Pernot M, Deffieux T, 2018. A large aperture row column addressed probe for in vivo 4D ultrafast doppler ultrasound imaging. *Phys. Med. Biol* 63, 215012. [PubMed: 30353889]
- Shanechi MM, 2019. Brain–machine interfaces from motor to mood. *Nat. Neurosci* 22, 1554–1564. [PubMed: 31551595]
- Shimoda K, Nagasaka Y, Chao ZC, Fujii N, 2012. Decoding continuous three-dimensional hand trajectories from epidural electrocorticographic signals in Japanese macaques. *J. Neural Eng* 9, 036015. [PubMed: 22627008]
- Sieu L-A, Bergel A, Tiran E, Deffieux T, Pernot M, Gennisson J-L, Tanter M, Cohen I, 2015. EEG and functional ultrasound imaging in mobile rats. *Nat. Methods* 12, 831. [PubMed: 26237228]
- Snyder LH, Batista AP, Andersen RA, 2000. Intention-related activity in the posterior parietal cortex: a review. *Vision Res.* 40, 1433–1441. [PubMed: 10788650]
- Snyder LH, Batista AP, Andersen RA, 1997. Coding of intention in the posterior parietal cortex. *Nature* 386, 167. [PubMed: 9062187]
- Soloukey S, Vincent AJ, Satoer DD, Mastik F, Smits M, Dirven CM, Strydis C, Bosch JG, van der Steen AF, De Zeeuw CI, 2020. Functional Ultrasound (fUS) During Awake Brain Surgery: The Clinical Potential of Intra-Operative Functional and Vascular Brain Mapping. *Front. Neurosci* 13, 1384. [PubMed: 31998060]
- Thier P, Andersen RA, 1998. Electrical microstimulation distinguishes distinct saccade-related areas in the posterior parietal cortex. *J. Neurophysiol* 80, 1713–1735. [PubMed: 9772234]
- Thier P, Andersen RA, 1996. Electrical microstimulation suggests two different forms of representation of head-centered space in the intraparietal sulcus of rhesus monkeys. *Proc. Natl. Acad. Sci* 93, 4962–4967. 10.1073/pnas.93.10.4962 [PubMed: 8643512]
- Urban A, Dussaux C, Martel G, Brunner C, Mace E, Montaldo G, 2015. Real-time imaging of brain activity in freely moving rats using functional ultrasound. *Nat. Methods* 12, 873–878. [PubMed: 26192084]
- Wang PT, Camacho E, Wang M, Li Y, Shaw SJ, Armacost M, Gong H, Kramer D, Lee B, Andersen RA, 2019. A benchtop system to assess the feasibility of a fully independent and implantable brain-machine interface. *J. Neural Eng* 16, 066043. [PubMed: 31585451]
- Wang PT, King CE, Chui LA, Do AH, Nenadic Z, 2012. Self-paced brain–computer interface control of ambulation in a virtual reality environment. *J. Neural Eng* 9, 056016. [PubMed: 23010771]
- Welle CG, Gao Y-R, Ye M, Lozzi A, Boretsky A, Abliz E, Hammer DX, 2020. Longitudinal neural and vascular structural dynamics produced by chronic microelectrode implantation. *Biomaterials* 238, 119831. 10.1016/j.biomaterials.2020.119831 [PubMed: 32045783]
- Wilke M, Kagan I, Andersen RA, 2012. Functional imaging reveals rapid reorganization of cortical activity after parietal inactivation in monkeys. *Proc. Natl. Acad. Sci* 109, 8274–8279. [PubMed: 22562793]
- Wolpaw JR, McFarland DJ, 2004. Control of a two-dimensional movement signal by a noninvasive brain-computer interface in humans. *Proc. Natl. Acad. Sci* 101, 17849–17854. [PubMed: 15585584]
- Wolpaw JR, McFarland DJ, Neat GW, Forneris CA, 1991. An EEG-based brain-computer interface for cursor control. *Electroencephalogr. Clin. Neurophysiol* 78, 252–259. [PubMed: 1707798]
- Woolley AJ, Desai HA, Otto KJ, 2013. Chronic intracortical microelectrode arrays induce non-uniform, depth-related tissue responses. *J. Neural Eng* 10, 026007. [PubMed: 23428842]

Highlights

- Functional ultrasound (fUS) images motor planning activity in non-human primates.
- fUS neuroimaging can predict single-trial movement timing, direction, and effector.
- This is a critical step toward less invasive and scalable brain-machine interfaces.

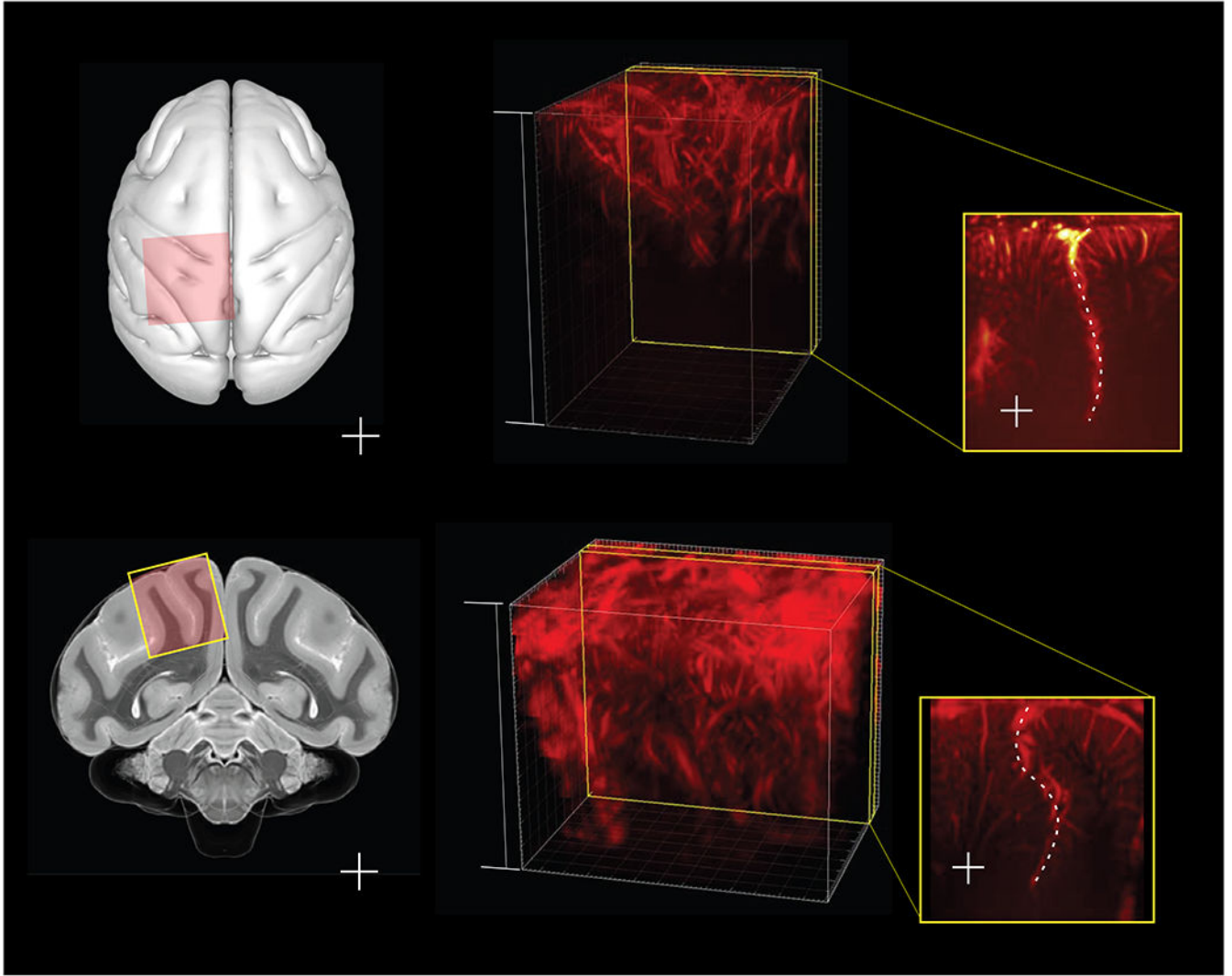


Fig. 1|. Anatomical scanning regions.

Illustrations of craniotomy field of view in **a**, axial plane and **b**, coronal cross-section, overlaid on a NHP brain atlas (Calabrese et al., 2015). The 24x24mm (inner dimension) chambers were placed surface normal to the brain on top of the craniotomized skull. **c**, **d**, 3D vascular maps for monkey L and monkey H. The field of view included the central and intraparietal sulci for both monkeys. **e**, **f**, Representative slices for monkey L and monkey H show the intraparietal sulcus (dotted line, labeled *ips*) with orientation markers (l=lateral or left, r=right, m=medial, v=ventral, d=dorsal, a=anterior, p=posterior).

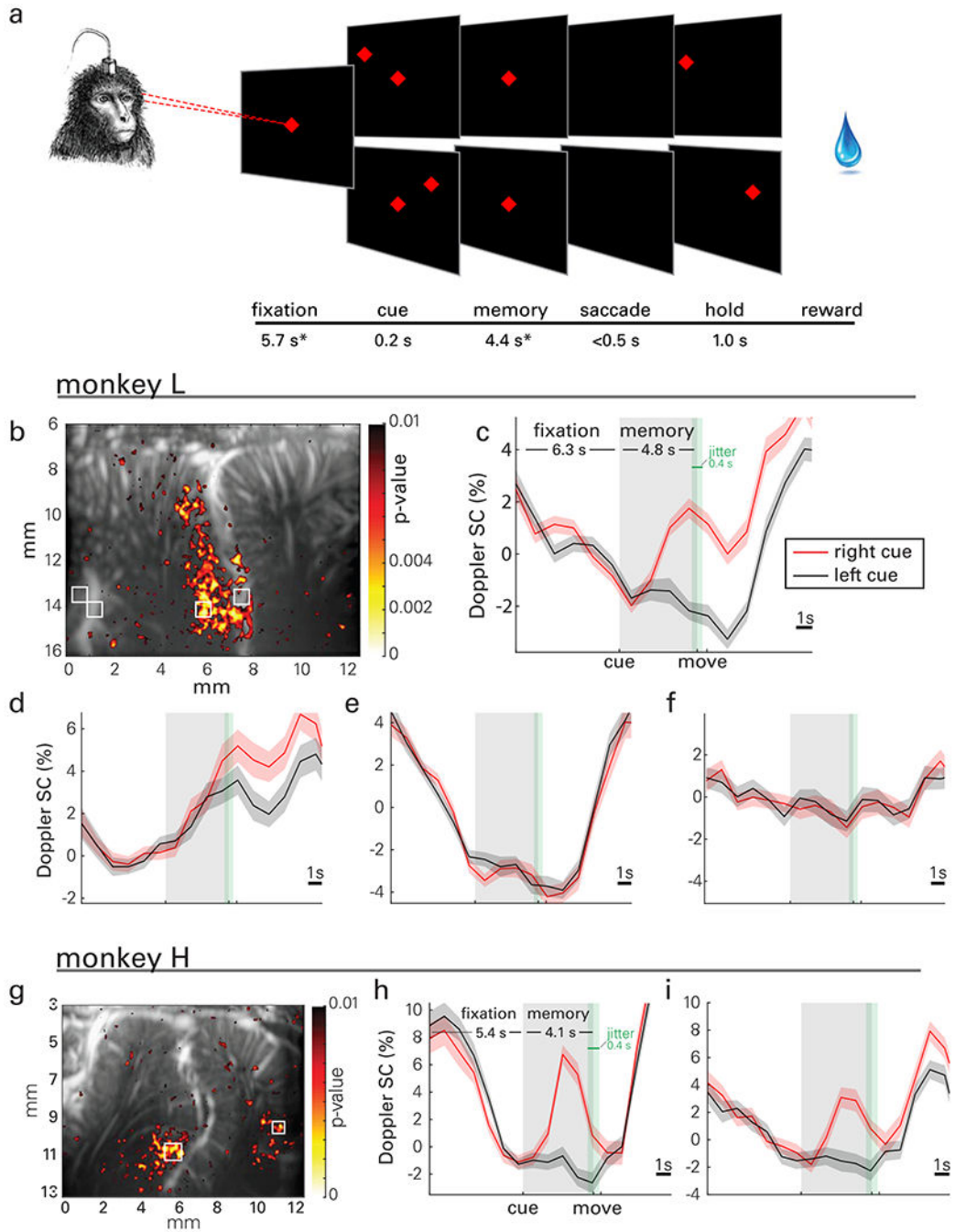
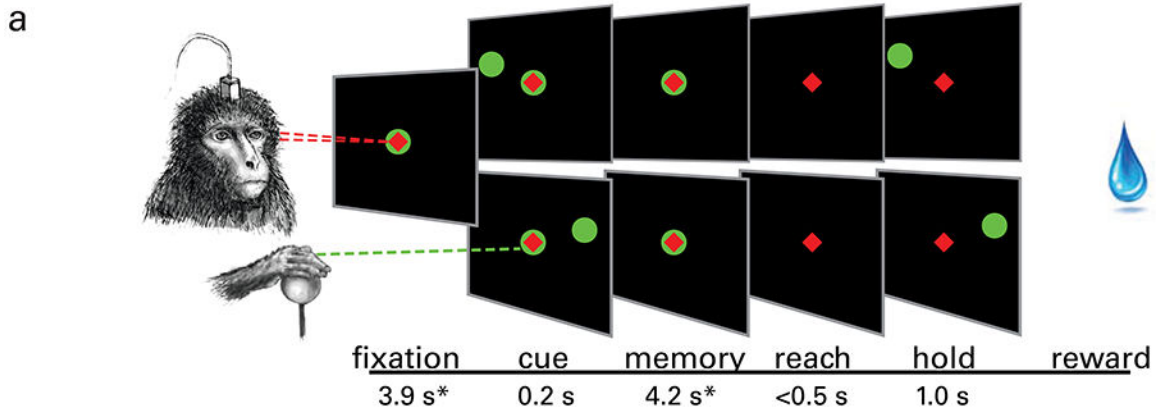


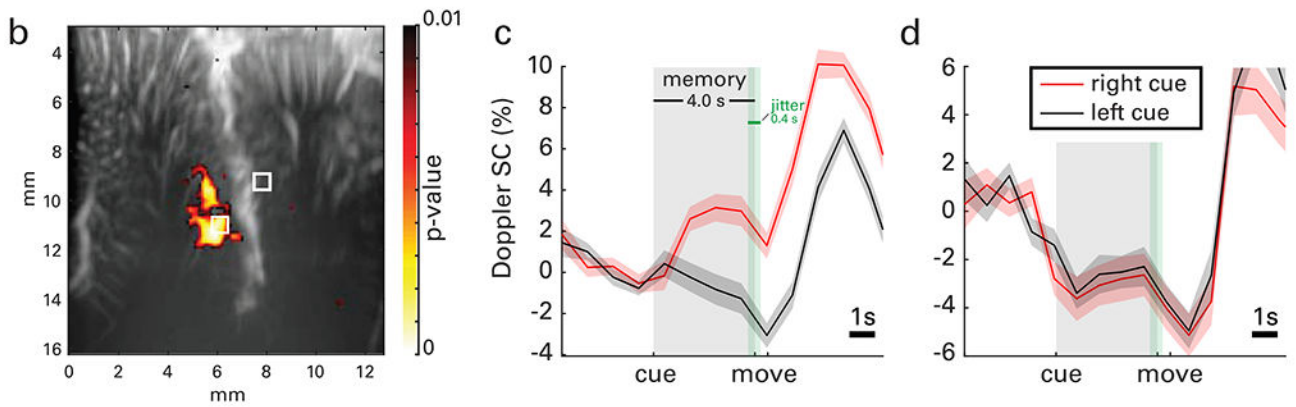
Fig. 2|. Saccade task, event-related response maps and waveforms.

a. A trial started with the animals fixating on a central cue (red diamond). Next, a target cue (red diamond) was flashed either on the left or the right visual field. During a memory period, the animals had to remember its location while continuing to fixate on the center cue. When the center was extinguished (go-signal), the animals performed a saccade to the remembered peripheral target location and maintained eye fixation before receiving a reward. *Mean values across sessions shown; the fixation and memory periods were consistent within each session but varied across sessions from 5.4-6.3 and 4.0-5.1 s,

respectively, depending on the animals' level of training. The fixation and memory periods were subject to 400 ms of jitter (green shaded area, uniform distribution) to preclude the animal from anticipating the change(s) of the trial phase. **b-f**, Representative activity map and event-related average (ERA) waveforms of CBV change during memory-guided saccades for monkey L. **g-i**, Activity map and ERA waveforms for monkey H. **b**, A statistical map shows localized areas with significantly higher signal change (SC) (one-sided t-test of area under the curve, $p < 0.01$) during the memory delay phase for right cued compared to left cued saccades, i.e., vascular patches of contralaterally tuned activity. **c, d**, ERA waveforms in LIP display lateralized tuning specific to local populations. **e**, Small vasculature outside of LIP exhibits event related structure that is tuned to task structure but not target direction. **f**, Vessels that perfuse large areas of cortex do not exhibit event related signal. **g**, Map for monkey H. **h**, ERA waveforms show lateralized tuning in LIP. **i**, Target tuning also appears in medial parietal area (MP) for monkey H. Panels c-f share a common range (9% signal change) as do h-i (14%). ERAs are displayed as means across trials and shaded areas represent standard error (s.e.m.).



monkey L



monkey H

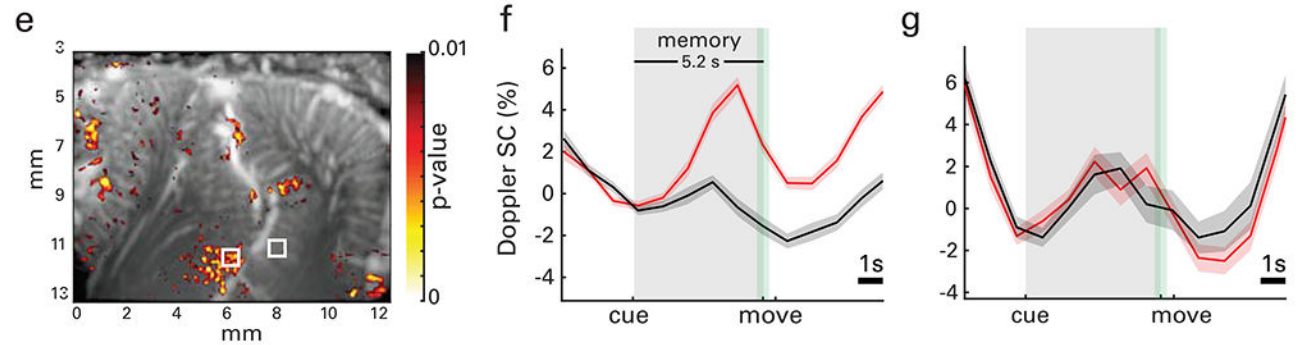


Fig. 3]. Reach task, event-related response map, waveforms, and decoding accuracy.

a, Monkeys performed a memory-guided reaching task using a 2D joystick. A trial started with the animal fixating on a central cue (red diamond) and positioning the joystick to its center (green circle). Next, a target (green circle) was flashed either on the left or the right visual field. The animal memorized its location while fixating eye and hand on the center cue. When the hand center cue was extinguished (go-signal), the animal performed a reach to the remembered target location and maintained the position before receiving a reward. Importantly, eye fixation was maintained throughout the entire trial. *Mean values across sessions shown; the fixation and memory periods were consistent within each session but

varied across sessions from 2.5-5.9 and 3.2-5.2 s, respectively. The fixation and memory periods were subject to 400 ms of jitter (green shaded area, uniform distribution) to preclude the animal from anticipating the change(s) of the trial phase. **b**, A statistical map shows localized areas with significantly higher signal change (SC) (one-sided t-test of area under the curve, $p < 0.01$, FDR corrected for number of pixels in image) during the memory delay phase for right cued compared to left cued reaches, i.e., vascular patches of contralaterally tuned activity. **c**, ERA waveforms from the lateral bank of *ips* reveal lateralized tuning in reaching movements. **d**, ERA waveforms in the medial bank of *ips* exhibit a population with bilateral tuning to reaching movements. ERAs are displayed as means across trials and shaded areas represent standard error (s.e.m.). **e-g**, Statistical map and ERA waveforms from monkey H.

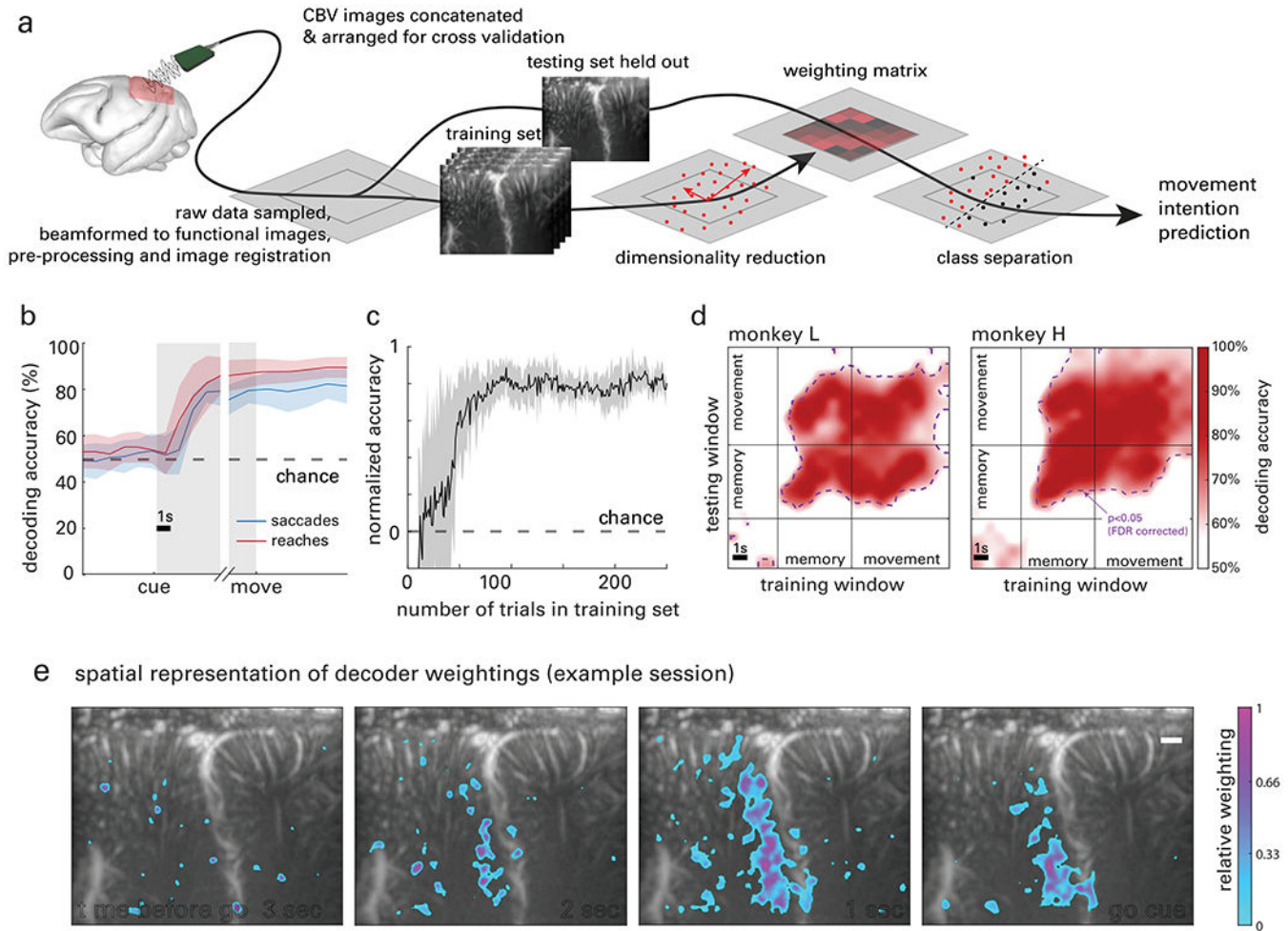


Fig. 4|. Single trial decoding.

a, Data flow chart for cross-validated single-trial movement direction decoding. Training images were separated from testing data according to the cross-validation technique being used. Movement intention predictions were made for single trials based on the dimensionality reduction and a classification model built by the training data with corresponding class labels, i.e., actual movement direction. **b**, Decoding accuracy as a function of time across all datasets. **c**, Decoding accuracy as a function of the number of trials used to train the decoder. Data points in **b** and **c** are means and shaded areas represent standard error (s.e.m.) across sessions. **d**, Cross-temporal decoder accuracy, using all combinations of training and testing data with a one second sliding window. Results are shown in an example session for each animal. Significance threshold is shown as a contour line ($p < 0.05$, FDR corrected). Training the classifiers during the memory or movement phase enabled successful decoding of the memory and movement phases. **e**, Representative decoder weighting maps (monkey L). The top 10% most heavily weighted voxels are shown as a function of space and time before the go cue was given, overlaid on the vascular map. See also Figure S1 and Supplementary Video.

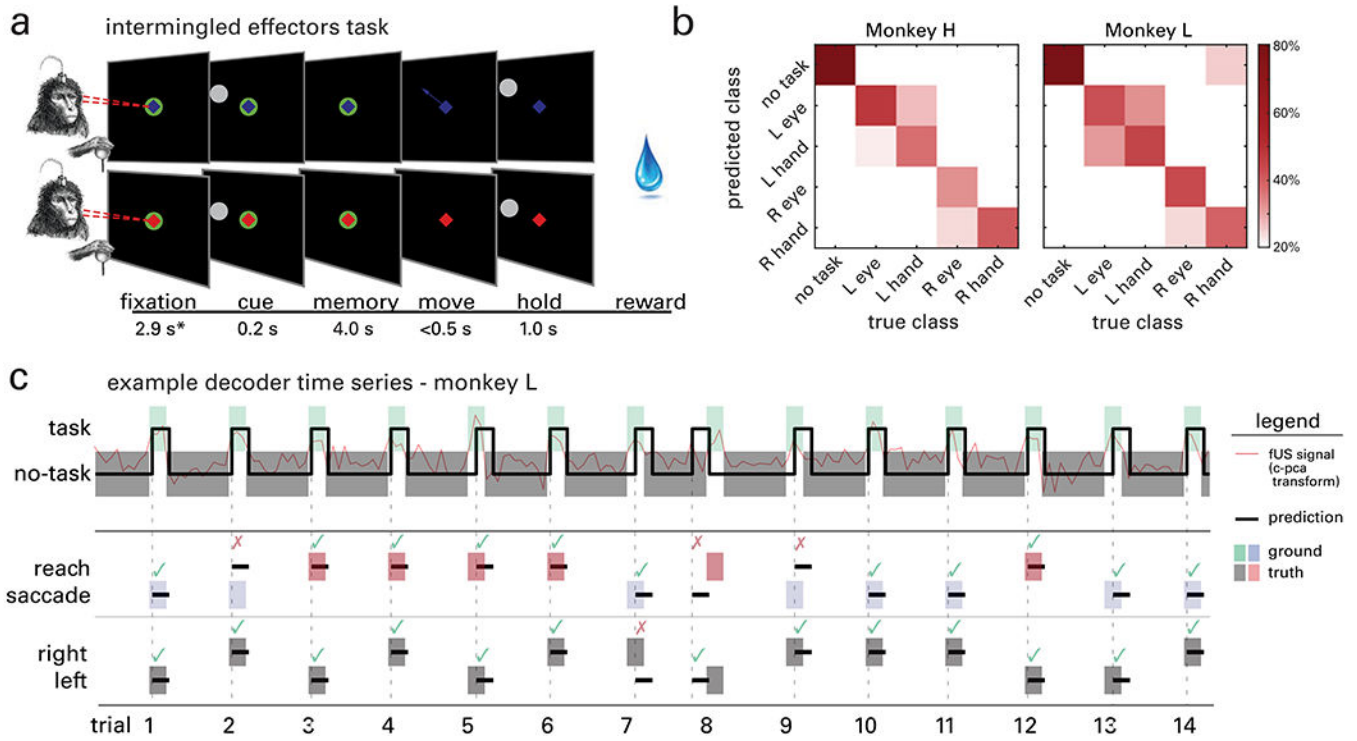


Fig. 5]. Decoding task, effector, and direction simultaneously.

a. Intermingled memory delayed saccade and reach task. A trial started with the animals fixating their gaze - and moving the joystick to - a central cue. The center fixation cue was either colored blue to cue saccades (top row) or red to cue reaches (bottom row), randomized trial-by-trial, i.e., not blocked. Next, a target (white circle) was flashed either on the left or the right visual field. The animals had to remember its location while continuing to fixate their eye and hand on the center cue. When the center was extinguished (go-signal), the animals performed a movement of either the eye or hand to the remembered peripheral target location. *Mean values across sessions shown; the fixation period was consistent within each session but varied across sessions from 2.4-4.3 s. **b.** Confusion matrices of decoding accuracy represented as percentage (columns add to 100%). **c.** Example classification of 14 consecutive trials. Classification predictions are shown as lines and shaded areas indicate ground truth. An example of the fUS image time series transformed by the classifier subspace appears in red. After predicting the task period, the classifier decoded effector (second row) and movement direction (third row) using data only from the predicted task period (first row).

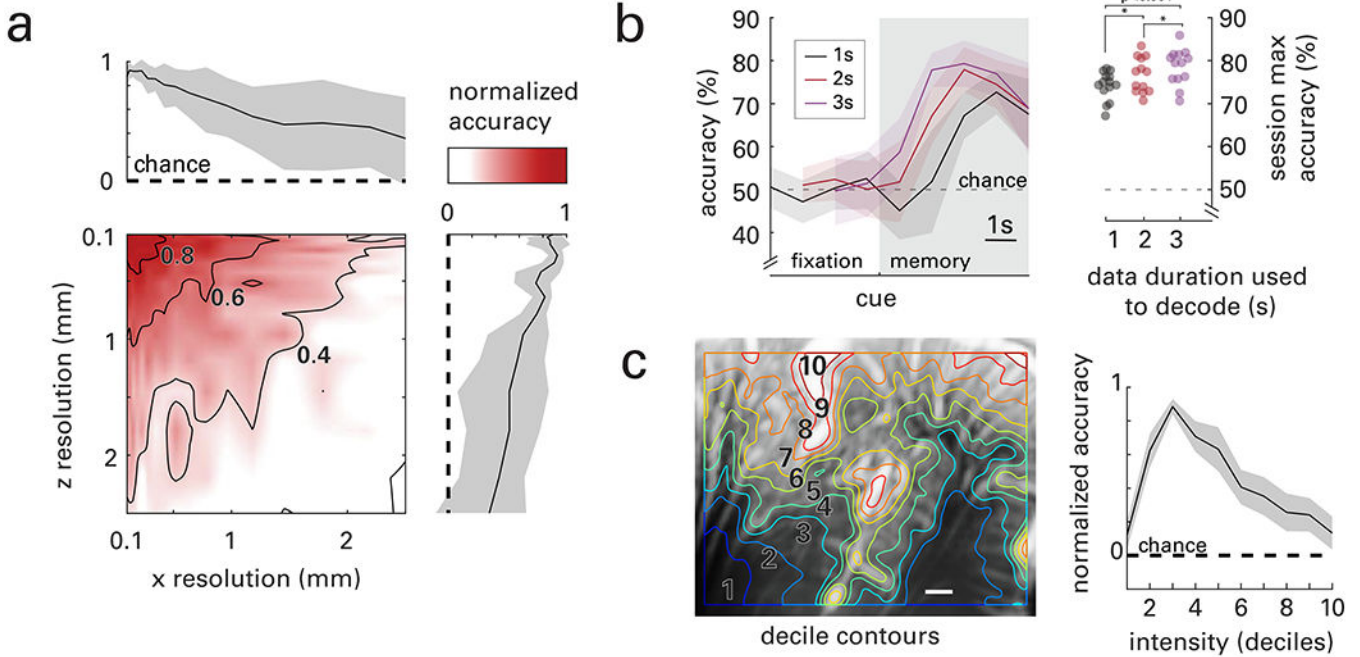


Fig. 6]. Effects of spatial resolution, time window, and mean power Doppler intensity.
a. Accuracy decreases with resolution in both the x-direction (across the imaging plane) and z-direction (depth in the plane) in an isotropic manner. **b.** Decoding accuracy as a function of decoder time bin durations (1, 2, and 3 second bins represented by black, red, and purple, respectively). Data are aligned to the end of the time bin used for decoding. Dots represent maximum decoder accuracy for each session for each of the bin sizes. Stars indicate statistical significance between groups (students t-test, $p < 0.001$ for all combinations). **c.** A typical vascular map overlaid with contours dividing the image into deciles of mean power Doppler intensity. Decoding accuracy is shown as a function of the mean power Doppler intensity. Information content is greatest in quantile 3 which mostly contains small vasculature within the cortex. Sub-cortical and primary unit vasculature (i.e., deciles 1 and 10) are least informative to decoding movement direction. All data represent means and shaded areas, when present, represent standard error (s.e.m.) across sessions.

KEY RESOURCES TABLE

REAGENT or RESOURCE	SOURCE	IDENTIFIER
Software and Algorithms		
Matlab 2020a	Mathworks	RRID:SCR_001622
Python Programming Language v2.7	Python Software Foundation	RRID:SCR_008394
PsychoPy v3.1.5	https://github.com/psychoopy/psychoopy	RRID:SCR_006571
Other		
Vantage 128 Research Ultrasound System	Verasonics	N/A
DOMINO linear array probe	Vernon	H.S.#901812000

Author Manuscript

Author Manuscript

Author Manuscript

Author Manuscript